

Bilayer graphene under pressure: Electron-hole Symmetry Breaking, Valley Hall Effect, and Landau Levels

F. Munoz,^{1,2} H. P. Ojeda Collado,^{3,4} Gonzalo Usaj,^{3,4} Jorge O. Sofo,⁵ and C. A. Balseiro^{3,4}

¹*Departamento de Física, Facultad de Ciencias, Universidad de Chile, Chile*

²*Centro para el Desarrollo de la Nanociencia y la Nanotecnología (CEDENNA), Santiago, Chile*

³*Centro Atómico Bariloche and Instituto Balseiro,*

Comisión Nacional de Energía Atómica, 8400 Bariloche, Argentina

⁴*Consejo Nacional de Investigaciones Científicas y Técnicas (CONICET), Argentina*

⁵*Department of Physics and Materials Research Institute,*

The Pennsylvania State University, University Park, Pennsylvania 16802, USA

The electronic structure of bilayer graphene under pressure develops very interesting features with an enhancement of the trigonal warping and a splitting of the parabolic touching bands at the K point of the reciprocal space into four Dirac cones, one at K and three along the T symmetry lines. As pressure is increased, these cones separate in reciprocal space and in energy, breaking the electron-hole symmetry. Due to their energy separation, their opposite Berry curvature can be observed in valley Hall effect experiments and in the structure of the Landau levels. Based on the electronic structure obtained by Density Functional Theory, we develop a low energy Hamiltonian that describes the effects of pressure on measurable quantities such as the Hall conductivity and the Landau levels of the system.

PACS numbers: 03.75.Lm, 72.25.Dc, 71.70.Ej

I. INTRODUCTION

Although the electronic structure of graphene has been known for more than half a century, it was the pioneer work of Novoselov and Geim in 2004 what triggered an impressive scientific and technological activity in this two-dimensional system.¹ Indeed the exceptional characteristics of graphene were fully revealed only after its systematic isolation, characterization and the first studies of its unusual mechanical, optical and transport properties.^{2–10} The band structure¹¹ includes two points at the corners K and K' of the Brillouin zone (BZ) that engender the peculiar low energy properties of the material. In fact, the low energy excitations around these points—the Dirac points—are described by chiral quasiparticles behaving as massless Dirac fermions leading to a number of remarkable phenomena.^{3,10,12,13}

Bilayer graphene (BLG) in the Bernal stacking consists of two graphene layers where only one of the two carbon atoms of the unit cell of the top layer lies on top of an atom of the bottom layer. The bilayer unit cell has four carbon atoms leading to four π -bands. Two of them touch each other at the Dirac points, having a parabolic dispersion relation with opposite curvature around it, which results in a zero band gap semiconductor. This simple-looking band structure wraps surprising properties that make BLG an exciting material from the point of view of exploring new physics and because of its potentials for technological applications.

The unique features emerging from the BLG electronic structure are due to different properties of the material. On the one hand an electric field perpendicular to the layers generates a tunable band gap,^{14–17} a required effect to engineer carbon-based semiconducting devices. On the other hand, from the topological point

of view,^{18,19} the Bloch wavefunctions of BLG present a rich behavior. Indeed by combining these two properties, the detection of the predicted generation of pure valley currents,²⁰ or valley-Hall effect,²¹ has been recently reported.²² The topological properties are determined by the Berry phase resulting from the winding of the phase of the Bloch wavefunction along a close path around the Dirac point.^{18,23–25} The consequences of a non-trivial Berry phase are diverse, in particular the mentioned valley-Hall effect results from the Berry curvature. In the presence of an external magnetic field, the structure of the Landau Levels (LLs) with a two-fold orbital degeneracy of the topologically protected zero energy ($n = 0$) levels of each valley is also due to the structure of the Berry phase.

Trigonal warping effects on BLG have also been extensively studied.^{3,26–28} They change the spectrum at low energies qualitatively generating four Dirac cones with zero energy around the K and K' points of the BZ. This is however a very small correction changing the spectrum in an energy range of a few meV around the Dirac points. It has been shown that distortions of the structure of BLG can be used to control and enhance the splitting of the parabolic band-contact point into the four cones that move away from the Dirac points.^{29,30} The way this splitting occurs is associated to topological invariants that define the LLs spectrum in the presence of an external magnetic field³¹ unveiling the richness of the electronic properties of BLG.

Here we present results for BLG under high pressure. We show that pressures in the range of 10 to 100 GPa modify in a substantial way the band structure around the Dirac points with the corresponding change of the wavefunctions and its topology. This is so because pressure changes the interlayer distance increasing the cou-

pling between layers. In the resulting band structure, the two parabolic bands evolve to generate four Dirac cones. One of them, with a marked trigonal warping is centered at the K (K') point and three elliptic cones move away towards the Γ point. The new ingredient, which has been overlooked in the past, is the breaking of the electron-hole symmetry. The energy of the trigonal cone apex at K is smaller than the energy of the apex of the three elliptical ones. This difference can be of the order of 0.1 eV and the Fermi surface of neutral BLG under pressure consists of small electron and hole pockets. In such a case, a large enough electric field opens an indirect gap. In other words, pressure induces a Lifshitz transition changing the nature of the Fermi surface that, depending on doping, may include electron and hole pockets, each one having a characteristic topological invariant (winding number). Although the pressure needed to observe these effects is rather high, this is still in the experimentally accessible range as, for small samples, diamond anvil cells can reach pressures³² much higher than the ones used in the present work.

We present the band structure and its evolution with pressure as obtained with Density Functional Theory (DFT). In particular, we analyze in detail the effect of pressure around the K and K' points of the BZ and present a tight-binding model that properly describes this effect. The microscopic parameters are obtained by fitting the DFT bands. We show that while the resulting electronic structure is topologically trivial, in the presence of an electric field the bands acquire a Berry curvature that lead to a non trivial pressure dependent valley Hall effect. We also present results for the LLs of BLG under pressure in the presence of an external magnetic field. These effects can be measured, adding to the rich behavior shown in BLG without pressure.³³

II. DFT CALCULATIONS

We will assume the Bernal stacking for which the unit cell has four carbon atoms, two in each plane. One of them is directly on top of an atom in the other plane (labeled A_1 and B_2 in Fig. 1) while the other two are on top of the hexagonal hole of the other plane (labeled A_2 and B_1 in the figure). We use DFT to determine the change of the atomic positions and the corresponding band structure with pressure, assuming that the effect of pressure is to reduce the distance between planes. To test the validity of this approximation, we used a more refined protocol considering that the isotropic pressure exerts equal force on each atom. This procedure is implemented by fixing the distance between atoms A_1 and B_2 and changing symmetrically the position perpendicular to the layers of atoms A_2 and B_1 (those opposed to the hexagon center on the other layer) until the force on them becomes equal to the force on the first pair. This procedure provides the structure corresponding to a uniform stress. We found that the difference between the results of this more re-

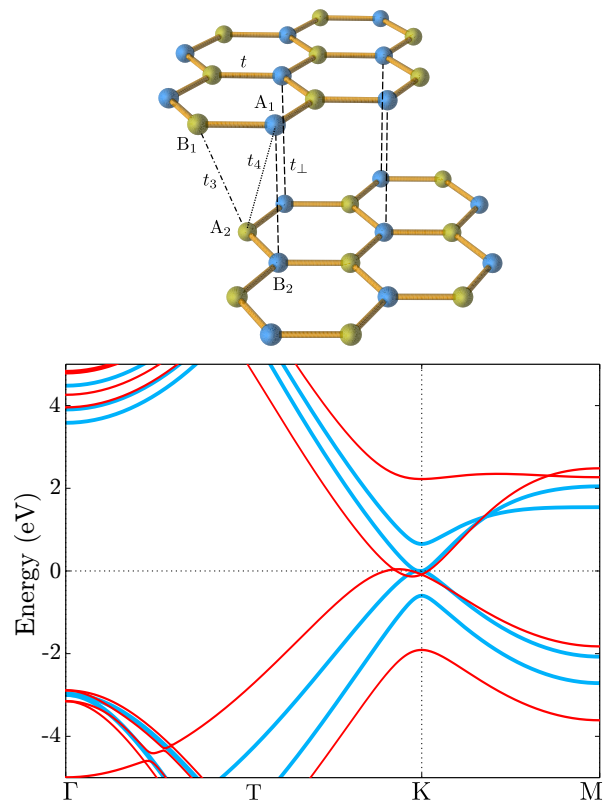


FIG. 1. (Color online) Top: The atomic structure of bilayer graphene in the Bernal stacking. Carbon atoms that are on top of each other are depicted in blue, while those aligned with the hexagonal hole in the other plane are depicted in green. Also shown in the figure are the hopping parameters used in our tight binding model. Bottom: Band structure along the $\Gamma \rightarrow K \rightarrow M$ path for two different pressures (12 and 96 GPa, thick light blue and thin red curves, respectively). There are four bands around the Fermi level (horizontal dashed line); two bands whose separation at K increases with increasing pressure and two that overlap (see Fig. 2).

finer procedure and those obtained using the rigid plane configuration was less than 0.025 Å at the largest pressure considered, leading to a negligible effect on the band structure. In what follows we present results from both procedures indistinguishably. The conversion from plane separation to pressure was determined from the forces on the atoms.

The DFT calculations were done using a plane wave basis set as implemented in the VASP code^{34–37} with an energy cutoff of 450 eV. The core electrons were treated with a frozen Projector Augmented Waves (PAW) scheme.^{38,39} The exchange and correlation functional was approximated with a simplified Generalized Gradient Approximation (GGA) as parametrized by Perdew, Burke, and Ernzerhof (PBE).^{40,41} Spin polarized calculations showed that in the range of experimentally accessible pressures the system is non-magnetic. Spin-orbit coupling was not included in this first runs. Given that the distance between the planes was a controlled parameter,

not derived from total energy minimization, the functional did not include van der Waals corrections.

Additional calculations were carried out to determine if the Bernal stacking is still the most stable BLG arrangement under pressure. We found that the Bernal stacking always corresponds to the minimum energy configuration—we will limit to this case from hereon. However, it is worth mentioning that a configuration with a lateral displacement with two top atoms symmetrically placed on top of a hexagon is very close in energy ($\Delta E = 15$ meV/atom at 71 GPa).

The important changes in the electronic structure of the bilayer under pressure occur in a very small region around the K point, which imposes a challenge to the numerical sampling of the Brillouin zone. A sampling of 300×300 , that in many cases would be enough to guarantee convergence in terms of BZ integration, is not enough to produce a reasonable determination of the Fermi level in the bilayer under pressure. To overcome this issue we used a non-uniform sampling with the equivalent of a 3000×3000 sampling in the neighborhood of the K point and a 300×300 grid in the rest of the BZ.

The band structure of BLG in the Bernal stacking is shown in the bottom panel of Fig. 1 for the lowest and highest pressures considered in this work. Around the K and K' points of the BZ, there are four low energy bands. At zero pressure, two bands touch with a parabolic dispersion relation at the Fermi level and two are separated by an energy proportional to the inter-plane hopping matrix element (t_\perp). As pressure is increased, the latter two bands separate more and more from the Fermi level, while the other two undergo a trigonal warping.

To display this trigonal warping in more detail, we plot the band structure for increasing pressure in the top panel of Fig. 2. With increasing pressure the parabolic dispersion relation of the low energy bands becomes a set of four Dirac cones,⁴² one that remains at K and three that shift in reciprocal space along the T path of the BZ. The energy of the Dirac points along the T lines increases with increasing pressure with respect to the point at K, reaching a value close to 100 meV at the highest pressure considered. A three-dimensional view of the bands at this pressure is shown in the bottom panel of Fig. 2.

The trigonal warping was mentioned before in tight binding models of the BLG.^{3,43,44} However, in all this models the Dirac cones along T remain at the same energy as the cone at K. As it is evident from the DFT results, with pressure there are extra ingredients that are missing in these tight binding representations. These important parameters are discussed in the next section where we present our tight binding model. The notable effect to be included is the electron hole symmetry breaking that enables the possibility to observe the Dirac cone splitting. Among its consequences are the charge transfer between sublattices *A* and *B* as well as the unveiling of interesting and measurable topological effects.

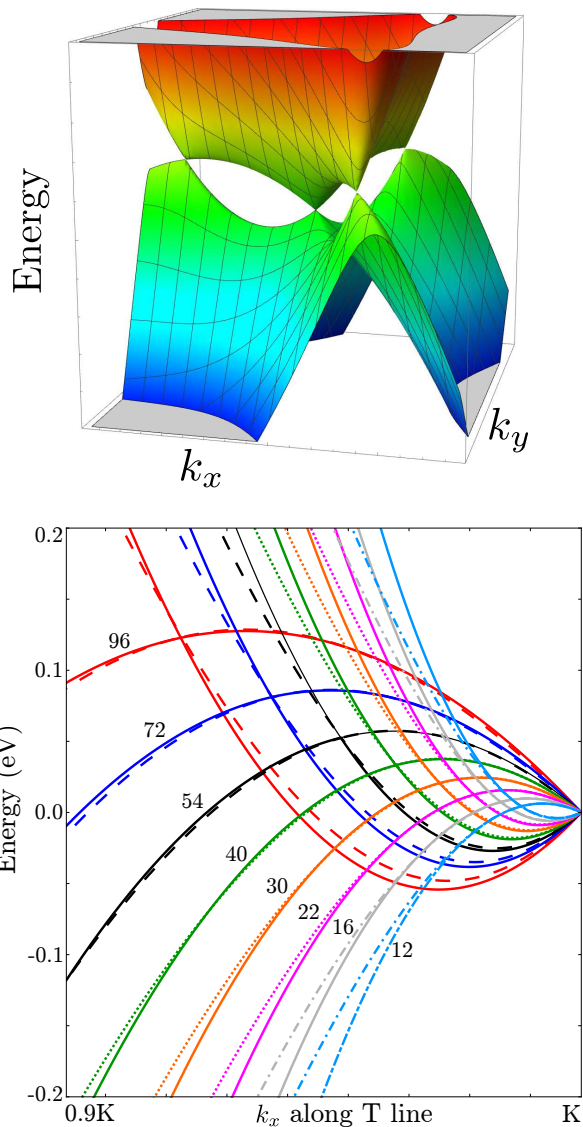


FIG. 2. Low energy band structure near the K point. Top: Band structure along the $\Gamma \rightarrow K$ path for different pressures (indicated in the figure in GPa). The effect of the trigonal warping and the electron-hole asymmetry increase as pressure is increased. The dashed lines show the fitting with the tight binding model described in Sec. III. Bottom: Detail of the four Dirac cones for a pressure of 96 GPa. Note that the energy of the Dirac point K (the central cone) is different from the other three.

III. TIGHT BINDING MODEL

A tight-binding approximation for the four bands close to the Fermi level of BLG has been discussed previously in the literature.^{43,44} We will use it now to describe the effect of pressure. As the latter increases, we will see that the hopping integral t_4 between atoms A_2 and A_1 (see Fig. 1) plays an increasingly important role: it is responsible for the electron-hole symmetry breaking and consequent energy separation of the Dirac cones at T

with respect to the cone at K. This important effect has been overlooked in the literature so far, mainly because the effect is negligible at low pressure.

The four bands around the Fermi level, which derive from the p_z orbitals, are described by the Hamiltonian $\mathcal{H} = \mathcal{H}_1 + \mathcal{H}_2 + \mathcal{H}_{12}$ where the first terms describes the electronic structure of the two graphene layers and the last one includes the inter-plane coupling

$$\mathcal{H}_i = - \sum_{\mathbf{k}, \sigma} (-1)^i \left[(\varepsilon + V) a_{i\mathbf{k}\sigma}^\dagger a_{i\mathbf{k}\sigma} + (-\varepsilon + V) b_{i\mathbf{k}\sigma}^\dagger b_{i\mathbf{k}\sigma} \right] - \sum_{\mathbf{k}, \sigma} t \left[\phi(\mathbf{k}) a_{i\mathbf{k}\sigma}^\dagger b_{i\mathbf{k}\sigma} + \phi(\mathbf{k})^* b_{i\mathbf{k}\sigma}^\dagger a_{i\mathbf{k}\sigma} \right], \quad (1)$$

with $i = 1, 2$. Here, $a_{i\mathbf{k}\sigma}$ and $b_{i\mathbf{k}\sigma}$ destroy electrons with wavevector \mathbf{k} and spin σ in sublattices A and B of the i -th plane, respectively, ε is the energy due to the charge transfer between the two sublattices on each plane, and we have included an electric field perpendicular to the BLG plane described by V . The matrix element t corresponds to the intra-plane hopping and

$$\phi(\mathbf{k}) = e^{iak_y} \left[1 + 2e^{-i\frac{3a}{2}k_y} \cos\left(\frac{a\sqrt{3}}{2}k_x\right) \right], \quad (2)$$

with the carbon-carbon distance $a = 1.42 \text{ \AA}$. The inter-plane coupling is described by

$$\begin{aligned} \mathcal{H}_{12} = & \sum_{\mathbf{k}, \sigma} t_\perp \left(a_{1\mathbf{k}\sigma}^\dagger b_{2\mathbf{k}\sigma} + b_{2\mathbf{k}\sigma}^\dagger a_{1\mathbf{k}\sigma} \right) \\ & + \sum_{\mathbf{k}, \sigma} t_3 \left(\phi(\mathbf{k}) b_{1\mathbf{k}\sigma}^\dagger a_{2\mathbf{k}\sigma} + \phi(\mathbf{k})^* a_{2\mathbf{k}\sigma}^\dagger b_{1\mathbf{k}\sigma} \right) \\ & + \sum_{\mathbf{k}, \sigma} t_4 \left(\phi(\mathbf{k})^* a_{1\mathbf{k}\sigma}^\dagger a_{2\mathbf{k}\sigma} + \phi(\mathbf{k}) a_{2\mathbf{k}\sigma}^\dagger a_{1\mathbf{k}\sigma} \right) \\ & + \sum_{\mathbf{k}, \sigma} t_4 \left(\phi(\mathbf{k})^* b_{1\mathbf{k}\sigma}^\dagger b_{2\mathbf{k}\sigma} + \phi(\mathbf{k}) b_{2\mathbf{k}\sigma}^\dagger b_{1\mathbf{k}\sigma} \right). \quad (3) \end{aligned}$$

Hence, for each value of the wave-number \mathbf{k} , we have a 4×4 Hamiltonian $H_{\mathbf{k}}$ given by

$$H_{\mathbf{k}} = \begin{pmatrix} \varepsilon + V & t\phi(\mathbf{k}) & t_4\phi^*(\mathbf{k}) & t_\perp \\ t\phi^*(\mathbf{k}) & -\varepsilon + V & t_3\phi(\mathbf{k}) & t_4\phi^*(\mathbf{k}) \\ t_4\phi(\mathbf{k}) & t_3\phi^*(\mathbf{k}) & -\varepsilon - V & t\phi(\mathbf{k}) \\ t_\perp & t_4\phi(\mathbf{k}) & t\phi^*(\mathbf{k}) & \varepsilon - V \end{pmatrix}, \quad (4)$$

with eigenvectors $[u_{A1}^n(\mathbf{k}), u_{B1}^n(\mathbf{k}), u_{A2}^n(\mathbf{k}), u_{B2}^n(\mathbf{k})]^T$ and eigenvalues $E_n(\mathbf{k})$ with $n = 1, 2, 3, 4$. This Hamiltonian, including t_4 has been written before⁴⁵ to study spin-orbit effects of BLG at zero pressure.

The low energy excitations with crystal momentum around the K and K' points of the BZ can be described by an effective two band Hamiltonian. The latter is obtained by eliminating the bands that are shifted from the Fermi energy by t_\perp . As pressure increases t_\perp also increases improving the range of validity of the approximation. Since we are interesting in describing the bands near the K point, we can measure \mathbf{k} from $\mathbf{K} = \frac{4\pi}{3\sqrt{3}a}(1, 0)$

so that $\phi(\mathbf{k}) \simeq -\frac{3a}{2}(k_x - ik_y)$ for $k = |\mathbf{k}| \ll |\mathbf{K}|$. In the base of the A_2 and B_1 orbitals, the effective Hamiltonian takes the form

$$H_{\mathbf{k}}^{\text{eff}} = e(k)I + \mathbf{h}(\mathbf{k}) \cdot \boldsymbol{\sigma}, \quad (5)$$

where I is the unit matrix, $\boldsymbol{\sigma} = (\sigma_x, \sigma_y, \sigma_z)$ with σ_i are the Pauli matrices,

$$e(k) = -\varepsilon + \alpha k^2 \quad (6)$$

and $\mathbf{h} = (h_x, h_y, h_z)$ with

$$\begin{aligned} h_x(\mathbf{k}) &= -\eta k_x + \beta(k_x^2 - k_y^2), \\ h_y(\mathbf{k}) &= \eta k_y + 2\beta k_x k_y, \\ h_z(\mathbf{k}) &= V. \end{aligned} \quad (7)$$

Here $\eta = 3t_3a/2$ and α and β are functions of microscopic parameters t, t_\perp, t_3 and t_4 . In the lowest order in V and ε we obtain

$$\alpha = \frac{9a^2}{2} \frac{tt_4}{t_\perp} \quad (8)$$

and

$$\beta = \frac{9a^2}{4} \frac{t^2 + t_4^2}{t_\perp}. \quad (9)$$

We have obtained the parameters of this effective two-band Hamiltonian by fitting the bands of the DFT calculations in the region around the K point. The results are provided in Table I and the resulting tight-binding bands are compared with the DFT-obtained bands in Fig. 2. Also in the table, we quote the results of measurements of the band structure of the BLG at normal pressure. All values of the parameters given in Table I are plotted in

TABLE I. Tight binding parameters for the effective two-band model of Eq. (5) obtained by fitting the bands of the DFT calculations. We include experimental values at normal pressure for comparison.

P (GPa)	α (eV \AA^2)	β (eV \AA^2)	η (eV \AA)
~ 0.1	16.81 ^a	133.97 ^a	0.00 ^a
~ 0.1	10.21 ^b	102.33 ^b	0.64 ^b
~ 0.1	10.53 ^c	127.40 ^c	0.21 ^c
11.6	10.895	49.815	-0.995
16.0	10.397	41.633	-1.114
21.9	9.950	36.236	-1.293
29.8	9.464	31.258	-1.470
40.1	8.917	26.922	-1.655
53.8	8.369	23.394	-1.866
71.9	7.796	20.375	-2.092
96.4	7.054	17.487	-2.324

^a Experimental values from Ref. [46].

^b Experimental values from Ref. [47].

^c Experimental values from Ref. [48].

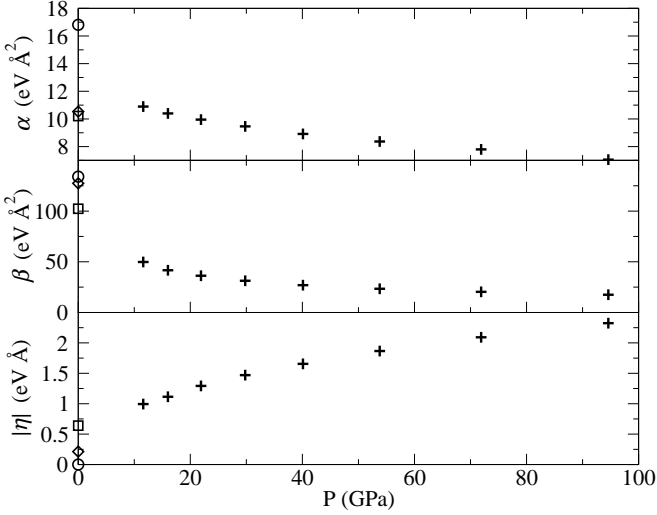


FIG. 3. Tight-binding parameters as function of pressure. (Plus signs) Values obtained by fitting the DFT-calculated bands along the T line of the Brillouin zone close to the point \mathbf{K} . (O) Experimental values from Ref. [46]. (□) Experimental values from Ref. [47]. (◇) Experimental values from Ref. [48].

Fig. 3 to show that the extrapolation of our theoretical values towards zero pressure falls well within the dispersion of the experimental values reported in the literature. We do not show calculated values at normal pressure because in this case, the inclusion of van der Waals corrections are very important. For higher pressures, the energy is dominated by the Pauli repulsion between planes and the absence of this corrections does not introduce any significant error.

Given this effective Hamiltonian, we can obtain the location of the four Dirac cones by finding the points in the BZ where $h_x = h_y = 0$ (assuming V is the smallest energy scale). One of the Dirac cones is always at $\mathbf{k} = (0, 0)$ and the other three are at $\mathbf{k} = \mathbf{T}_i$ with $i = 1, 2, 3$ and

$$\begin{aligned} \mathbf{T}_1 &= \left(\frac{\eta}{\beta}, 0 \right), \\ \mathbf{T}_2 &= \frac{\eta}{\beta} \left(-\frac{1}{2}, \frac{\sqrt{3}}{2} \right), \\ \mathbf{T}_3 &= \frac{\eta}{\beta} \left(-\frac{1}{2}, -\frac{\sqrt{3}}{2} \right). \end{aligned} \quad (10)$$

By linearizing the effective Hamiltonian $H_{\mathbf{k}}^{\text{eff}}$ for a small separation \mathbf{q} from these points we reveal the band structure at these Dirac cones and obtain expressions that facilitate the evaluation of its topological properties and their consequences. Around $\mathbf{k} = (0, 0)$ (K point) we then have

$$h_x(\mathbf{q}) \simeq -\eta q_x, \quad h_y(\mathbf{q}) \simeq \eta q_y, \quad e(\mathbf{q}) \simeq -\varepsilon, \quad (11)$$

which gives the following eigenenergies

$$E_{\mathbf{K}}^{\pm}(\mathbf{q}) = -\varepsilon \pm \sqrt{V^2 + \eta^2 (q_x^2 + q_y^2)}. \quad (12)$$

Similarly, around \mathbf{T}_1 we find that

$$\begin{aligned} h_x(\mathbf{T}_1 + \mathbf{q}) &\simeq \eta q_x, \\ h_y(\mathbf{T}_1 + \mathbf{q}) &\simeq 3\eta q_y, \\ e(\mathbf{T}_1 + \mathbf{q}) &\simeq -\varepsilon + \alpha \frac{\eta^2}{\beta^2} + 2\alpha \frac{\eta}{\beta} q_x, \end{aligned} \quad (13)$$

and the corresponding eigenenergies

$$E_{\mathbf{T}_1}^{\pm}(\mathbf{q}) = -\varepsilon + \alpha \frac{\eta^2}{\beta^2} + 2\alpha \frac{\eta}{\beta} q_x \pm \sqrt{V^2 + \eta^2 (q_x^2 + 9q_y^2)}. \quad (14)$$

Expressions for \mathbf{T}_2 and \mathbf{T}_3 are similar and can be obtained by symmetry considerations or by direct calculation.

It is clear from Fig. 2 that there are four characteristic energies that define the low energy band structure (taking $V = 0$): $E_{\mathbf{K}}^{\pm}(\mathbf{0}) = -\varepsilon$, corresponding to the apex of the Dirac cone centred at K, the energy $E_{\mathbf{T}_1}^{\pm}(\mathbf{0})$ of the apex of the cones shifted from K and the energies E_{sv} and E_{sc} of the saddle points (relative minimum and maximum) of the valence and conduction bands, respectively. These four energies divide the energy-pressure plane in five different regions (see Fig. 4). In each of them the surface of constant energy consists of different pieces with different topological properties. For neutral BLG, the Fermi energy is larger than $E_{\mathbf{K}}^{\pm}(\mathbf{0})$ and smaller than $E_{\mathbf{T}_1}^{\pm}(\mathbf{0})$ and the 2D Fermi surface consists of an electron pocket centred at \mathbf{K} and three hole pockets centred at \mathbf{T}_i and its symmetrically equivalent points. The same occurs around the \mathbf{K}' point of the BZ.

Comparing the band energies at \mathbf{K} and at \mathbf{T}_1 we obtain

$$E_{\mathbf{T}_1}^{\pm}(\mathbf{0}) - E_{\mathbf{K}}^{\pm}(\mathbf{0}) = \alpha \frac{\eta^2}{\beta^2} \propto t_4, \quad (15)$$

which is proportional to t_4 . This lead us to an important point: *without including this term in the tight binding model, the trigonal warping does not separate the cones in energy and leads to the wrong conclusion that their individual properties would not manifested in transport or spectroscopic experiments.* This is not the case as we show in the following sections.

IV. BERRY CURVATURE AND VALLEY HALL EFFECT

The interesting band topology of BLG unveiled by the effect of pressure offers a unique possibility to study valley polarization and the valley Hall effect.²¹ In contrast to the graphene case, this system only requires to apply a small electric field perpendicular to the bilayer to reveal this phenomena. In this section we will use our previously developed tight-binding model to evaluate the Berry curvature of the bands and the transverse conductivity as a function of pressure.

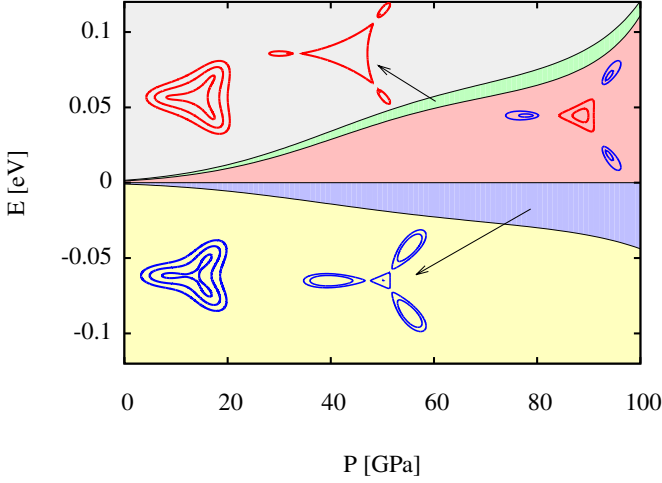


FIG. 4. (Color online) The (E,P) plane with the four lines defining regions with different topology of the Fermi lines, in each region the form of constant energy curves are shown, blue and red lines indicate the portions corresponding the valence and conduction bands respectively.

With the four band Hamiltonian of Eq. (4), the Berry curvature of the n -th band is given by

$$\Omega_z^n = 2 \text{Im} \sum_{n' \neq n} \frac{\langle n | \frac{\partial H_{\mathbf{k}}}{\partial k_x} | n' \rangle \langle n' | \frac{\partial H_{\mathbf{k}}}{\partial k_y} | n \rangle}{(E_n(\mathbf{k}) - E_{n'}(\mathbf{k}))^2}. \quad (16)$$

This expression, however, requires a simple but nonetheless unnecessary numerical work. Since the Berry curvature is concentrated around the location of the Dirac cones, we can use the two band approximation of Eqs. (5), (6), and (7) to calculate the Berry curvature of these bands.⁴⁹ In this case¹⁸

$$\Omega_z^\pm = \mp \frac{1}{2h^3} \mathbf{h} \cdot \partial_{k_x} \mathbf{h} \times \partial_{k_y} \mathbf{h} \quad (17)$$

where $h^3 = (h_x^2 + h_y^2 + h_z^2)^{3/2}$. This finally gives

$$\Omega_z^\pm = \frac{\mp V [4\beta^2 k^2 - \eta^2]}{2 [\beta^2 k^4 + \eta k^2 + 2\eta\beta k_x (2k_y^2 - k_x^2) + V^2]^{3/2}}, \quad (18)$$

where $k^2 = k_x^2 + k_y^2$. The intrinsic contribution to the anomalous Hall effect is given by²³

$$\sigma_{xy} = \frac{e^2}{\hbar} \int \frac{d\mathbf{k}}{(2\pi)^2} \sum_{s=\pm} f(E_s(\mathbf{k})) \Omega_z^s(\mathbf{k}). \quad (19)$$

Given that the curvature is substantially large around the conical intersections compared with its value around other regions of the BZ, we can use the approximated expressions around \mathbf{K} and \mathbf{T}_1 to simplify this expression. To a good degree of approximation this conductivity can be calculated as

$$\sigma_{xy} = \sigma_{\mathbf{K}} + \sum_{i=1}^3 \sigma_{\mathbf{T}_i} = \sigma_{\mathbf{K}} + 3\sigma_{\mathbf{T}_1} \quad (20)$$

where we have used the symmetry of the three \mathbf{T}_i points and have defined

$$\sigma_{\mathbf{K}} = \frac{e^2}{\hbar} \int \frac{d\mathbf{q}}{(2\pi)^2} \sum_{s=\pm} f(E_{\mathbf{K}}^s(\mathbf{q})) \Omega_z^s(\mathbf{q}) \quad (21)$$

and

$$\sigma_{\mathbf{T}_1} = \frac{e^2}{\hbar} \int \frac{d\mathbf{q}}{(2\pi)^2} \sum_{s=\pm} f(E_{\mathbf{T}_1}^s(\mathbf{q})) \Omega_z^s(\mathbf{T}_1 + \mathbf{q}). \quad (22)$$

The integration around the \mathbf{K} point can be done analytically at zero temperature using the approximation (obtained from Eq. (18))

$$\Omega_z^\pm(\mathbf{q}) \simeq \pm \frac{V\eta^2}{2(V^2 + \eta^2 q^2)^{3/2}}, \quad (23)$$

so that its contribution to the conductivity results

$$\sigma_{\mathbf{K}} = \begin{cases} \frac{e^2}{2\hbar} \frac{V}{\mu + \varepsilon} & \mu < -\varepsilon - V \\ -\frac{e^2}{2\hbar} & -\varepsilon - V < \mu < -\varepsilon + V \\ -\frac{e^2}{2\hbar} \frac{V}{\mu + \varepsilon} & \mu > -\varepsilon + V \end{cases} \quad (24)$$

where μ is the chemical potential. Around \mathbf{T}_1 we can use that

$$\Omega_z^\pm(\mathbf{T}_1 + \mathbf{q}) \simeq \mp \frac{3V\eta^2}{2(V^2 + \eta^2 q_x^2 + 9\eta^2 q_y^2)^{3/2}}. \quad (25)$$

In this case, however, the presence of q_x outside the square root in the energy, Eq. (14), makes the integration rather difficult. Nevertheless, the contribution to the conductivity from this region of the BZ can be approximated as

$$\sigma_{\mathbf{T}_1} = \begin{cases} -\frac{e^2}{2\hbar} \frac{V}{\mu - E_0} & \mu < E_0 - V \\ \frac{e^2}{2\hbar} & E_0 - V < \mu < E_0 + V \\ +\frac{e^2}{2\hbar} \frac{V}{\mu - E_0} & \mu > E_0 + V \end{cases}, \quad (26)$$

where $E_0 = -\varepsilon + \alpha \frac{\eta^2}{\beta^2}$ is the center of the band gap opened by the perpendicular electric field.

We can now calculate the expected variation with applied pressure of the total intrinsic contribution to the anomalous Hall conductivity as a function of the chemical potential as shown in Fig. 5. In this figure we see that with increasing pressure the contribution from the cones at the \mathbf{T}_i points moves to higher energies and produces an anomalous Hall conductivity that is three times larger, and of opposite sign, than the contribution (observed at lower μ) produced by the cone at \mathbf{K} . Close to zero pressure, our approximations are bound to be worst because the Dirac cones at \mathbf{T}_1 are closer to \mathbf{K} . However, in this figure it is clear that the anomalous conductivity as the pressure becomes smaller tends the values for BLG at zero pressure.³³ This dramatic change with pressure, made possible by the electron-hole symmetry breaking, can have interesting applications as a very sensitive

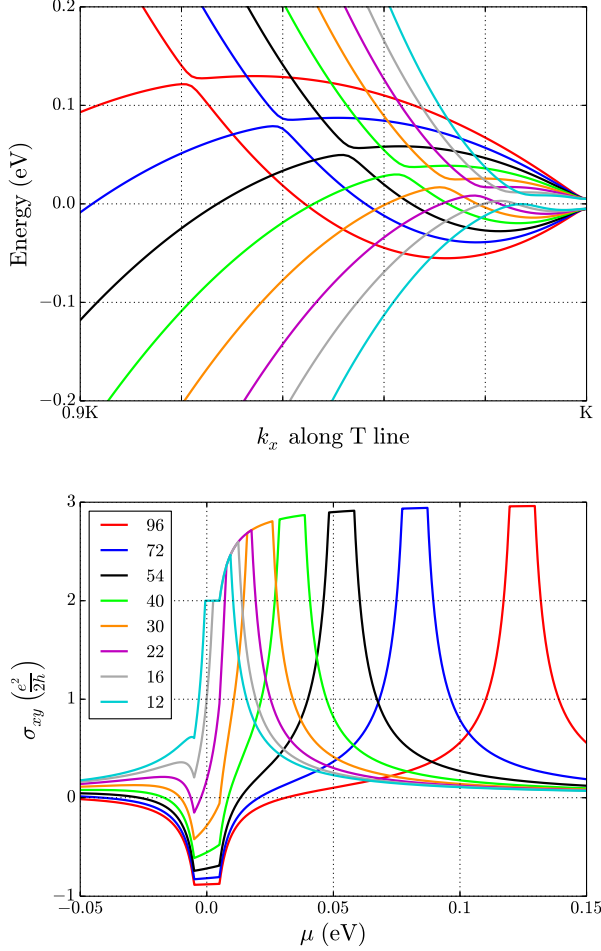


FIG. 5. (Upper panel) Energy bands of the bilayer at different pressures under the effect of an electric field perpendicular to the bilayer equivalent to $V = 0.005$ eV. (Bottom panel) Intrinsic contribution to the anomalous Hall conductivity as function of the chemical potential for different applied pressures and the same applied field.

pressure gauge. Apart from the already interesting phenomena of the direct observation of a valley hole effect in BLG, it is important to highlight that the signature of this effect will be the ratio of 3 to 1 as the chemical potential is swipes through the gaps at \mathbf{K} and \mathbf{T}_1 .

V. LANDAU LEVELS

The LLs in BLG have received much attention during the last decade.^{50,51} The simplest description in the absence of electric fields predicts a spectrum with two-fold zero energy states (per spin) for each one of the Dirac cones at the \mathbf{K} and the \mathbf{K}' points of the BZ. The trigonal warping, given by the parameter β (that preserves the electron-hole symmetry), strongly modifies the spectrum at low fields. In fact, as we showed in the previous

sections, this perturbation modifies the parabolic bands around the Dirac points leading to four degenerate cones in each corner of the BZ. As a consequence, for low magnetic fields the zero energy states at \mathbf{K} (\mathbf{K}') have a four-fold degeneracy (per spin). Pressure breaks electron-hole symmetry shifting the energy of the cones and removes some of the degeneracies of the low energy LLs. Moreover, as we show below, all states have a field dependent energy. The robustness of the zero energy LL characteristic of monolayer and multilayer graphene is lost in the high pressure regime.

To calculate the Landau Levels of BLG under pressure we proceed as in Refs. [30] and [52]. In the continuous limit and in the presence of an external magnetic field \mathbf{B} the canonical momentum \mathbf{p} must be replaced by $\mathbf{\Pi} = \mathbf{p} + e\mathbf{A}(\mathbf{r})$ where $\mathbf{A}(\mathbf{r})$ is the vector potential describing a magnetic field perpendicular to the graphene layers. We use units such that $\hbar \equiv 1 \equiv c$. The components of the gauge-invariant momentum obey the commutation relation $[\Pi_x, \Pi_y] = -i/l_B^2$ where $l_B \simeq 26\text{nm}/\sqrt{B[\text{T}]}$ is the magnetic length. This allows us to introduce the harmonic oscillator operators $\hat{a} = \lambda^{-1}\Pi_-$ and $\hat{a}^\dagger = \lambda^{-1}\Pi_+$ with $[\hat{a}, \hat{a}^\dagger] = 1$, $\lambda = (l_B/\sqrt{2})^{-1}$ and where $\Pi_\pm = \Pi_x \pm i\Pi_y$. In what follows we use the Landau gauge $\mathbf{A}(\mathbf{r}) = (0, Bx)$. Then, the effective two band Hamiltonian takes the form

$$H = \begin{pmatrix} -\varepsilon + \alpha\lambda^2\hat{a}^\dagger\hat{a} & -\eta\lambda\hat{a} + \beta\lambda^2\hat{a}^{\dagger 2} \\ -\eta\lambda\hat{a}^\dagger + \beta\lambda^2\hat{a}^2 & -\varepsilon + \alpha\lambda^2\hat{a}\hat{a}^\dagger \end{pmatrix}. \quad (27)$$

As usual, in the base of Landau functions $\psi(x, y) = e^{iky}\varphi_n(x)$ the harmonic oscillator operator satisfy

$$\begin{aligned} \hat{a}^\dagger\varphi_n &= \sqrt{n+1}\varphi_{n+1} \\ \hat{a}\varphi_n &= \sqrt{n}\varphi_{n-1}. \end{aligned} \quad (28)$$

With the minimum inter-plane coupling, $\alpha = \eta = 0$ and the charge transfer energy $\varepsilon = 0$, the model reduces to the simplest model used to describe BLG at room pressure. In this case the LLs spectrum contains a zero energy doublet and states with energies $E_n^\pm = \pm\sqrt{n(n-1)}\hbar\omega_c$ with $n \geq 2$ and $\hbar\omega_c = \beta\lambda^2$. The corresponding wavefunctions are

$$\chi_0 = \begin{bmatrix} \varphi_0 \\ 0 \end{bmatrix}, \quad \chi_1 = \begin{bmatrix} \varphi_1 \\ 0 \end{bmatrix}, \quad \chi_n^\pm = \begin{bmatrix} \varphi_n \\ \pm\varphi_{n-2} \end{bmatrix}. \quad (29)$$

For small pressure the LLs energies are shifted by a first order correction due to the α -terms in Hamiltonian (27). These corrections break the electron-hole symmetry and lift the degeneracy of the zero energy modes. The first-order corrected spectrum has $E_0 = 0$, $E_1 = \alpha\lambda^2$ and, for $n \geq 2$, $E_n = \pm\sqrt{n(n-1)}\hbar\omega_c + (2n-1)\alpha\lambda^2$. This effect can be observed in Fig. 6(a). Further second order corrections due to the η and α terms were also evaluated. However, as the pressure increases, perturbation theory is not enough to account for the evolution of the LLs spectrum. The numerically obtained spectrum for different pressures is shown in the left panels of Fig. 6.

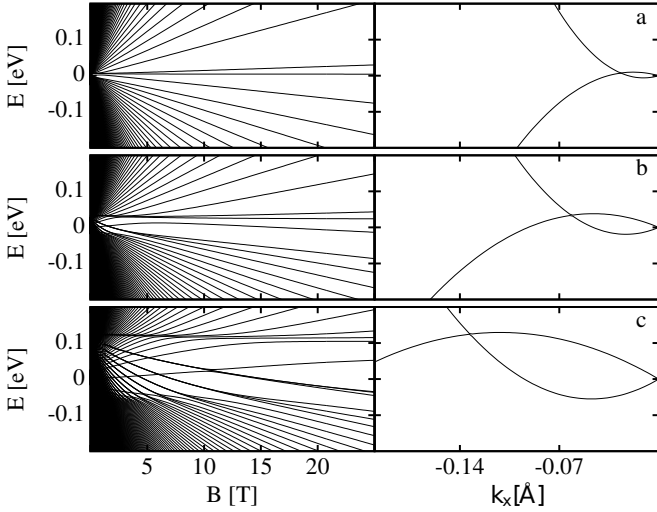


FIG. 6. Left and right panels correspond to the LLs spectrum and the zero field band structure, respectively, for different values of pressure: (a) 16 GPa; (b) 40 GPa; (c) 96 GPa.

For high pressures and low energies ($E_{sv} < E < E_{sc}$) we can get some insight into the structure of the LLs spectrum by assuming the presence of four independent Dirac cones, centered at the \mathbf{K} and \mathbf{T}_i points. The corresponding spectrum is given by $E_{\mathbf{K},n} = E_{\mathbf{K},0} \pm C_1 \sqrt{Bn}$ and $E_{\mathbf{T}_1,n} = E_{\mathbf{T}_1,0} \pm C_2 \sqrt{Bn}$ where C_1 and C_2 are constants. While the structure of the so obtained LLs spectrum is similar to the numerically obtained results, there are important differences (see Fig. 7). First, in the numerical results, it is evident that the energies of the $n = 0$ LL states of the four cones are no longer field independent—quantum corrections for the low n states are important even for small fields. In addition, there are anticrossings that cannot be captured by in a picture that treats the cones independently. We also notice that as the energy of the upper cone LLs approach the saddle point energy E_{sv} , the three fold degeneracy is lifted. These last effects

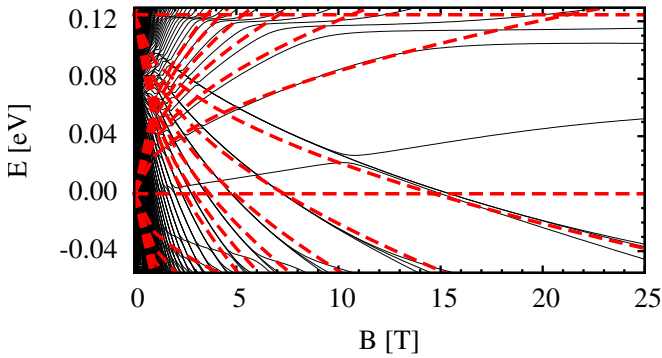


FIG. 7. (Color online) LLs spectrum obtained numerically for 96 GPa (continuous black lines) and LLs spectrum corresponding to two independent Dirac cone centered at \mathbf{K} and \mathbf{T}_1 (dashed red lines).

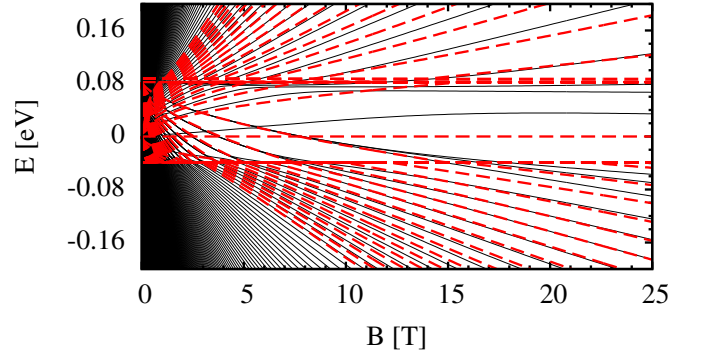


FIG. 8. (Color online) Comparison between LLs spectrum obtained numerically (continuous black lines) and using Onsager's quantization (dashed red lines), see Eq. (30), under 72 GPa.

are due to the magnetic breakdown, *i.e.* Landau-Zener tunneling mixing the states of the different cones.

A similar and more qualitative analysis can be done by resorting to the Onsager's semiclassical quantization rule.⁵³ This rule states that the area enclosed by orbits in k -space are quantized according to the following condition³¹

$$A(E_m) = 2\pi e B(m + \gamma). \quad (30)$$

Here E_m is the energy of the orbit and γ is a constant ($0 \leq \gamma < 1$) independent of the quantum number m . Onsager's semiclassical approach is well justified for large m only. However, for the sake of comparison, we shall use it without restriction, including the $m = 0$ states. Concerning the quantization condition of Eq. (30) it was recently shown that, in two band materials like the one under consideration, the constant γ is given by the pseudo-spin winding number w_C which is $1/\pi$ times the Berry phase obtained along the close orbit³¹

$$\gamma = \frac{1}{2} - \frac{|w_C|}{2}. \quad (31)$$

After evaluation the areas as a function of the energy and calculating the winding numbers corresponding to the different constant energy close-orbits, we invert Eq. (30) to obtain the semiclassical spectrum. The comparison of the semiclassical and the numerical results shown in Fig. 8 is quite good for not too small values of n . The LLs corresponding to small n do not follow Onsager's rule. Moreover, the numerical results show that all LLs have a field dependent energy showing that in the presence of the electron-hole symmetry breaking parameter α the stability of the zero-modes LL is lost.

Finally, the LLs spectrum in the presence of a perpendicular electric field $V = 50\text{meV}$ is shown in Fig. 9 for different pressures. With the minimum inter-layer coupling ($t_3 = t_4 = 0$), any electric field opens a gap and the LLs spectrum displays such a gap with a set of LLs associated to the conduction band, whose energies increase

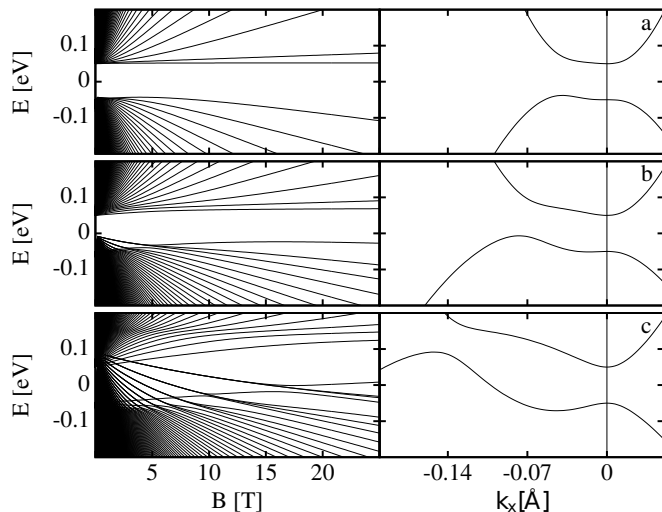


FIG. 9. The same that Fig. 6 but in the presence of a perpendicular electric field $V = 50\text{meV}$.

with increasing magnetic field, separated from those corresponding to the valence band with opposite slope. As the pressure increases the gap decreases and for a given (electric field dependent) critical pressure the gap closes as a consequence of the band crossing as discussed in the previous section.

VI. SUMMARY AND CONCLUSIONS

We have shown that upon the application of pressure the low energy band structure of BLG undergoes an interesting transformation. Two parabolic bands touching at the \mathbf{K} point of the Brillouin zone with phase winding 2π transform into a set of four Dirac cones, one with a winding number of π that remains at \mathbf{K} and three that separate along the \mathbf{T} lines with a winding number of $-\pi$. The most interesting discovery is that the cones at \mathbf{T} separate in energy from the cone at \mathbf{K} generating a Lifshitz transition visible by experiment. The study of the electronic structure using DFT and the interpretation of the results in terms of a tight-binding model show that the main effects of pressure are the following: (i) an increase of the direct A_1B_2 hopping integrals t_\perp . As a result, two bands are shifted away from the Dirac point improving the description of the system in terms of an effective two band model; (ii) an increase of the t_3 and t_4 hopping integrals. These parameters modify the low energy band structure generating four Dirac cones at the two corners

of the BZ. An important effect is the breaking of the electron-hole symmetry; and (iii) a small charge transfer between the two non-equivalent sites of each plane, an effect that is not relevant when describing the low energy bands in terms of a simple two band model.

The resulting band structure is summarized in Fig. 4 where the energy-pressure plane is divided in five regions with different constant energy surfaces. Our estimates of the pressure dependence of the microscopic parameters are in good agreement with the zero pressure extrapolation as obtained in recent experimental works.

The evolution of the band structure with pressure can be measured by means of different experimental techniques. Although the small buckling of the graphene planes with pressure does not produce a significant increase of the spin-orbit coupling, valley Hall effect and the structure of the Landau levels show important changes unveiling the pressure induced Lifshitz transition.

We presented results of the Hall conductivity and show that this quantity is very sensitive to the pressure and to the carrier density. Variations in the Fermi level change the sign and the magnitude of the valley Hall response that is increased by a factor three as the carriers vary their origin from the single Dirac cone at \mathbf{K} to the triple degenerate Dirac cones at \mathbf{T} . The high sensitivity of this effect with pressure makes this structure a potential source for the design of a device for the detection of small pressure variations on two dimensional surfaces such as screen devices and joints.

The LLs evolve from a simple structure at low pressures to a rich spectrum at high pressures. The most notable effect is the breaking of the electron-hole symmetry and the lack of stability of the zero-LL modes, whereas all modes have a field dependent energy.

ACKNOWLEDGMENTS

FM is supported by ‘Financiamiento Basal para Centros Científicos y Tecnológicos de Excelencia FB 0807’ and Fondecyt grant # 1150806. JOS and CAB are grateful to the American Physical Society International Travel Grant Awards Program that supported the visit of CAB to Penn State when this work was started. HPOC, GU and CAB acknowledge financial support from PICTs 2013-1045 and Bicentenario 2010-1060 from ANPCyT, PIP 11220110100832 from CONICET and grant 06/C415 from SeCyT-UNC. GU acknowledges support from the ICTP associateship program and the Simons Foundation.

¹ K. S. Novoselov, A. K. Geim, S. V. Morozov, D. Jiang, Y. Zhang, S. V. Dubonos, I. V. Grigorieva, and A. A. Firsov, “Electric Field Effect in Atomically Thin Carbon Films,” *Science* **306**, 666 (2004).

² Y. Zhang, Y.-W. Tan, H. L. Stormer, and P. Kim, “Experimental observation of the quantum hall effect and and berry’s phase in graphene,” *Nature* **438**, 201 (2005).

³ A. H. Castro Neto, F. Guinea, N. M. R. Peres, K. S.

- Novoselov, and A. K. Geim, “The electronic properties of graphene,” *Rev. Mod. Phys.* **81**, 109 (2009).
- ⁴ A. A. Balandin, S. Ghosh, W. Bao, I. Calizo, D. Teweldebrhan, F. Miao, and C. N. Lau, “Superior thermal conductivity of single-layer graphene,” *Nano Lett.* **8**, 902 (2008).
 - ⁵ F. Bonaccorso, Z. Sun, T. Hasan, and A. C. Ferrari, “Graphene photonics and optoelectronics,” *Nat. Photon.* **4**, 611 (2010).
 - ⁶ K. S. Novoselov, A. K. Geim, S. V. Morozov, D. Jiang, M. I. Katsnelson, I. V. Grigorieva, S. V. Dubonos, and A. A. Firsov, “Two-dimensional gas of massless Dirac fermions in graphene,” *Nature* **438**, 197 (2005).
 - ⁷ M. I. Katsnelson, K. S. Novoselov, and A. K. Geim, “Chiral tunnelling and the Klein paradox in graphene,” *Nat. Phys.* **2**, 620 (2006).
 - ⁸ K. S. Novoselov, Z. Jiang, Y. Zhang, S. V. Morozov, H. L. Stormer, U. Zeitler, J. C. Maan, G. S. Boebinger, P. Kim, and A. K. Geim, “Room-temperature quantum Hall effect in graphene,” *Science* **315**, 1379 (2007).
 - ⁹ A. K. Geim and A. H. MacDonald, “Graphene: Exploring carbon flatland,” *Phys. Today* **60**, 35 (2007).
 - ¹⁰ S. Das Sarma, S. Adam, E. H. Hwang, and E. Rossi, “Electronic transport in two-dimensional graphene,” *Rev. Mod. Phys.* **83**, 407 (2011).
 - ¹¹ P. Wallace, “The band theory of graphite,” *Phys. Rev.* **71**, 622 (1947).
 - ¹² C. W. J. Beenakker, “Colloquium: Andreev reflection and klein tunneling in graphene,” *Rev. Mod. Phys.* **80**, 1337 (2008).
 - ¹³ M. O. Goerbig, “Electronic properties of graphene in a strong magnetic field,” *Rev. Mod. Phys.* **83**, 1193 (2011).
 - ¹⁴ E. V. Castro, K. S. Novoselov, S. V. Morozov, N. M. R. Peres, Lopes J. M. B. dos Santos, J. Nilsson, F. Guinea, A. K. Geim, and A. H. Castro Neto, “Biased Bilayer Graphene: Semiconductor with a Gap Tunable by the Electric Field Effect,” *Phys. Rev. Lett.* **99**, 216802 (2007).
 - ¹⁵ E. McCann, “Asymmetry gap in the electronic band structure of bilayer graphene,” *Phys. Rev. B* **74**, 161403 (2006).
 - ¹⁶ H. Min, B. Sahu, S. K. Banerjee, and A. H. MacDonald, “Ab initio theory of gate induced gaps in graphene bilayers,” *Phys. Rev. B* **75**, 155115 (2007).
 - ¹⁷ T. Taychatanapat and P. Jarillo-Herrero, “Electronic transport in dual-gated bilayer graphene at large displacement fields,” *Phys. Rev. Lett.* **105**, 166601 (2010).
 - ¹⁸ M. Z. Hasan and C. L. Kane, “Colloquium: Topological insulators,” *Rev. Mod. Phys.* **82**, 3045 (2010).
 - ¹⁹ I. Martin, Y. M. Blanter, and A. F. Morpurgo, “Topological confinement in bilayer graphene,” *Phys. Rev. Lett.* **100**, 036804 (2008).
 - ²⁰ A. Rycerz, J. Tworzydło, and C. W. J. Beenakker, “Valley filter and valley valve in graphene,” *Nat. Phys.* **3**, 172 (2007).
 - ²¹ D. Xiao, W. Yao, and Q. Niu, “Valley-Contrasting Physics in Graphene: Magnetic Moment and Topological Transport,” *Phys. Rev. Lett.* **99**, 236809 (2007).
 - ²² M. Sui, G. Chen, L. Ma, W.-Y. Shan, D. Tian, K. Watanabe, T. Taniguchi, X. Jin, W. Yao, D. Xiao, and Y. Zhang, “Gate-tunable topological valley transport in bilayer graphene,” *Nat Phys* **11**, 1027 (2015).
 - ²³ D. Xiao, M.-C. Chang, and Q. Niu, “Berry phase effects on electronic properties,” *Rev. Mod. Phys.* **82**, 1959 (2010).
 - ²⁴ Y. Ando, “Topological insulator materials,” *J. Phys. Soc. Jpn.* **82**, 102001 (2013).
 - ²⁵ Y. Ren, Z. Qiao, and Q. Niu, “Topological phases in two-dimensional materials: A brief review,” *ArXiv e-prints* (2015), arXiv:1509.09016.
 - ²⁶ K. Kechedzhi, V. I. Fal’ko, E. McCann, and B. L. Altshuler, “Influence of trigonal warping on interference effects in bilayer graphene,” *Phys. Rev. Lett.* **98**, 176806 (2007).
 - ²⁷ J. Cserti, A. Csordás, and G. Dávid, “Role of the trigonal warping on the minimal conductivity of bilayer graphene,” *Phys. Rev. Lett.* **99**, 066802 (2007).
 - ²⁸ M. Koshino and E. McCann, “Trigonal warping and Berry’s phase $N\pi$ in ABC-stacked multilayer graphene,” *Phys. Rev. B* **80**, 165409 (2009).
 - ²⁹ G. Montambaux, F. Piéchon, J.-N. Fuchs, and M. O. Goerbig, “Merging of Dirac points in a two-dimensional crystal,” *Phys. Rev. B* **80**, 153412 (2009).
 - ³⁰ R. de Gail, M. O. Goerbig, and G. Montambaux, “Magnetic spectrum of trigonally warped bilayer graphene: Semiclassical analysis, zero modes, and topological winding numbers,” *Phys. Rev. B* **86**, 045407 (2012).
 - ³¹ J. N. Fuchs, F. Piéchon, M. O. Goerbig, and G. Montambaux, “Topological Berry phase and semiclassical quantization of cyclotron orbits for two dimensional electrons in coupled band models,” *Eur. Phys. J. B* **77**, 351 (2010).
 - ³² P. F. McMillan, “New materials from high-pressure experiments,” *Nat. Mater.* **1**, 19 (2002).
 - ³³ K. S. Novoselov, E. McCann, S. V. Morozov, V. I. Fal’ko, M. I. Katsnelson, U. Zeitler, D. Jiang, F. Schedin, and A. K. Geim, “Unconventional quantum Hall effect and Berry’s phase of 2π in bilayer graphene,” *Nat Phys* **2**, 177 (2006).
 - ³⁴ G. Kresse and J. Hafner, “Ab initio molecular dynamics for liquid metals,” *Phys. Rev. B* **47**, 558 (1993).
 - ³⁵ G. Kresse and J. Hafner, “Ab initio molecular-dynamics simulation of the liquid-metal-amorphous-semiconductor transition in germanium,” *Phys. Rev. B* **49**, 14251 (1994).
 - ³⁶ G. Kresse and J. Furthmüller, “Efficiency of ab-initio total energy calculations for metals and semiconductors using a plane-wave basis set,” *Comput. Mater. Sci.* **6**, 15 (1996).
 - ³⁷ G. Kresse and J. Furthmüller, “Efficient iterative schemes for ab initio total-energy calculations using a plane-wave basis set,” *Phys. Rev. B* **54**, 11169 (1996).
 - ³⁸ P. E. Blöchl, “Projector augmented-wave method,” *Phys. Rev. B* **50**, 17953 (1994).
 - ³⁹ G. Kresse and D. Joubert, “From ultrasoft pseudopotentials to the projector augmented-wave method,” *Phys. Rev. B* **59**, 1758 (1999).
 - ⁴⁰ J. P. Perdew, K. Burke, and M. Ernzerhof, “Generalized Gradient Approximation Made Simple,” *Phys. Rev. Lett.* **77**, 3865 (1996).
 - ⁴¹ J. P. Perdew, K. Burke, and M. Ernzerhof, “Generalized Gradient Approximation Made Simple [Phys. Rev. Lett. **77**, 3865 (1996)],” *Phys. Rev. Lett.* **78**, 1396 (1997).
 - ⁴² It should be emphasize that trigonal warping effects are always present, even a zero pressure. However, in such a case they occur at much lower energy, since the t_3 and t_4 hopping parameters (see next section) are rather small. In the first approximation, we take this limit as if $t_3 = t_4 = 0$.
 - ⁴³ E. McCann, D. S. L. Abergel, and V. I. Fal’ko, “Electrons in bilayer graphene,” *Solid State Commun.* **143**, 110 (2007).
 - ⁴⁴ J. Nilsson, A. H. Castro Neto, F. Guinea, and N. M. R. Peres, “Electronic properties of bilayer and multilayer graphene,” *Phys. Rev. B* **78**, 045405 (2008).

- ⁴⁵ S. Konschuh, M. Gmitra, D. Kochan, and J. Fabian, "Theory of spin-orbit coupling in bilayer graphene," *Phys. Rev. B* **85**, 115423 (2012).
- ⁴⁶ K. Zou, X. Hong, and J. Zhu, "Effective mass of electrons and holes in bilayer graphene: Electron-hole asymmetry and electron-electron interaction," *Phys. Rev. B* **84**, 085408 (2011).
- ⁴⁷ L. M. Zhang, Z. Q. Li, D. N. Basov, M. M. Fogler, Z. Hao, and M. C. Martin, "Determination of the electronic structure of bilayer graphene from infrared spectroscopy," *Phys. Rev. B* **78**, 235408 (2008).
- ⁴⁸ L. M. Malard, J. Nilsson, D. C. Elias, J. C. Brant, F. Plentz, E. S. Alves, A. H. Castro Neto, and M. A. Pimenta, "Probing the electronic structure of bilayer graphene by Raman scattering," *Phys. Rev. B* **76**, 201401 (2007).
- ⁴⁹ We have compared the result of calculating the Berry curvature from the 4×4 model and the 2×2 approximation and the difference is negligible.
- ⁵⁰ L.-J. Yin, Y. Zhang, J.-B. Qiao, S.-Y. Li, and L. He, "Experimental Observation of Surface States and Landau Levels Bending in Bilayer Graphene," arXiv:1510.06109 [cond-mat] (2015), arXiv: 1510.06109.
- ⁵¹ T. Kawarabayashi, Y. Hasugai, and H. Aoki, "Stability of zero-mode Landau levels in bilayer graphene against disorder in the presence of the trigonal warping," *J. Phys.: Conf. Ser.* **456**, 012020 (2013).
- ⁵² S. Yuan, R. Roldán, and M. I. Katsnelson, "Landau level spectrum of ABA- and ABC-stacked trilayer graphene," *Phys. Rev. B* **84**, 125455 (2011).
- ⁵³ L. Onsager, "Interpretation of the de Haas-van Alphen Effect," *Phil. Mag.* **43**, 1006 (1952).